

This is the accepted manuscript made available via CHORUS. The article has been published as:

## Intradomain Textures in Block Copolymers: Multizone Alignment and Biaxiality

Ishan Prasad, Youngmi Seo, Lisa M. Hall, and Gregory M. Grason

Phys. Rev. Lett. **118**, 247801 — Published 12 June 2017

DOI: [10.1103/PhysRevLett.118.247801](https://doi.org/10.1103/PhysRevLett.118.247801)

# Intradomain Textures in Block Copolymers: Multizone Alignment and Biaxiality

Ishan Prasad

*Department of Chemical Engineering, University of Massachusetts, Amherst, Massachusetts 01003, USA*

Youngmi Seo and Lisa M. Hall

*William G. Lowrie Department of Chemical and Biomolecular Engineering,  
The Ohio State University, Columbus, Ohio 43210, USA*

Gregory M. Grason

*Department of Polymer Science and Engineering,  
University of Massachusetts, Amherst, MA 01003, USA*

Block copolymer (BCP) melt assembly has been studied for decades, focusing largely on self-organized spatial patterns of periodically-ordered segment density. Here, we demonstrate that underlying the well-known composition profiles (i.e. ordered lamella, cylinders, spheres and networks) are generic and heterogeneous patterns of segment orientation that couple strongly to morphology, even in the absence of specific factors that promote intra- or inter-chain segment alignment. We employ both self-consistent field theory and coarse-grained simulation methods to measure polar and nematic order parameters of segments in a freely-jointed chain model of diblock melts. We show that BCP morphologies have a *multizone* texture, with segments predominantly aligned normal and parallel to inter-domain interfaces in the respective brush and interfacial regions of the microdomain. Further, morphologies with anisotropically-curved interfaces (i.e. cylinders and networks) exhibit biaxial order that is aligned to the principal curvature axes of the interface.

Block copolymer (BCP) melts assemble into a rich array of periodic morphologies [1] depending on chain composition, architecture, and interactions [2–4]. Over the past several decades, investigations of BCP assembly have focused on equilibrium composition profiles of chemical segments  $\phi_\alpha(\mathbf{x})$  (for component  $\alpha$ ) and their connection to molecular architecture [5]. Periodically-ordered morphologies break not only continuous translational symmetries of a disordered melt, but also its continuous rotational symmetry. As a consequence, they necessarily possess orientational order, at both the scale of micro-domain lattice and the sub-domain scale. Despite the extensive study of the spatially-ordered composition profiles of BCP and their now widespread applications in nanotechnology [6], knowledge of the orientational order of chain segments that underlies these spatial patterns is conspicuously lacking.

In this Letter we use self-consistent field (SCF) theory and coarse-grained simulations to analyze intra-domain segment orientation patterns in BCP melts to understand i) in which directions constituent segments orient within ordered microdomains; and ii) how alignment varies with BCP morphology. Our analysis is based on the simplest models of flexible BCPs, which lack both explicit and implicit orientational interaction between segments, but nonetheless exhibit generic textures of orientational order. Studies of liquid-crystalline textures of small molecules confined to volumes of differing micro-/nano-size, shape, and topology (e.g. droplets [7, 8] to 3D periodic networks [9]) show that such textures are highly dependent on the shape of the confining volume, orientational symmetries of the ordered phases [10, 11], and,

crucially, the anchoring of alignment at the confining surface [12]. Analogous alignment may be expected from the spontaneously formed interface between unlike components, posing a basic question, do segments align parallel (homogeneous) or normal (homeotropic) to inter-domain surfaces? Curiously, SCF studies of the nematic order parameter in phase-separated mixtures of homopolymers show a generic tendency of segmental alignment parallel to the interface over the interfacial width [13–15], while the SCF prediction of the polar order in BCP microdomains shows instead a normal alignment more characteristic of a SmA-like order [16, 17]. Here, we show that *both* normal and parallel segment alignment coexist generically within BCP microdomains, albeit in different spatial regions. We describe the principles that control relative strengths and directionality alignment in different BCP morphologies and in different subregions of a given morphology. Perhaps most surprising, we report the generic emergence of biaxial segment order in morphologies with anisotropically-curved interfaces.

We consider a freely-jointed chain model of a diblock copolymer melt [18], where chains possess  $N_A = fN$  and  $N_B = (1 - f)N$  segments of  $A$ - and  $B$ -type monomers, respectively, with equal segment length  $a$  and volume  $\rho_0^{-1}$ . In the mean-field (or SCF) approximation, chain conformations are encoded in end-distribution functions,  $q^+(n, \mathbf{x})$  and  $q^-(n, \mathbf{x})$ , which describe the statistical weights of disjoint sections of the chain from the respective  $A$  ( $n = 0$ ) and  $B$  ( $n = N$ ) ends to reach  $\mathbf{x}$  at the  $n$ th segment [5]. Thus, the probability (per unit volume) of the  $n$ th segment of the diblock at  $\mathbf{x}$  is  $\rho(\mathbf{x}, n) = q^+(n, \mathbf{x})q^-(n, \mathbf{x})/Z$ , where  $Z$  is the single-chain

partition function  $Z = \int d^3\mathbf{x} q^+(n, \mathbf{x}) q^-(n, \mathbf{x})$ . The mean-field scalar order parameters, volume fractions of  $A$  and  $B$ , follow directly from the end-distributions

$$\phi_\alpha(\mathbf{x}) = \left\langle \rho_0^{-1} \sum_{\nu \in \alpha} \delta(\mathbf{x}_\nu - \mathbf{x}) \right\rangle = \frac{V}{N} \int_\alpha dn \rho(\mathbf{x}, n), \quad (1)$$

where  $\nu \in \alpha$  labels all segments of type  $\alpha = A$  or  $B$ . Due to random-walk chain statistics [19], end distributions obey the modified diffusion equation [5, 20, 21],

$$\pm \frac{\partial q^\pm}{\partial n} = \frac{a^2}{6} \nabla^2 q^\pm - w(n, \mathbf{x}) q^\pm, \quad (2)$$

where  $w(n, \mathbf{x}) = \Theta(N_A - n)w_A(\mathbf{x}) + \Theta(n - N_A)w_B(\mathbf{x})$ , with  $w_{A/B}(\mathbf{x})$  the spatially-varying chemical potential field for  $A$  or  $B$  generated by local segment (scalar) interactions [22]. The chemical potential fields satisfy the mean-field, self-consistency, condition,  $w_{A/B}(\mathbf{x}) = \chi \phi_{B/A}(\mathbf{x}) + \xi(\mathbf{x})$ , where Flory parameter,  $\chi$ , describes repulsive interactions between unlike species and the pressure field,  $\xi(\mathbf{x})$ , acts on both species to maintain constant density (i.e.  $\phi_A(\mathbf{x}) + \phi_B(\mathbf{x}) = 1$ ). Equilibrium states are determined by solving eq.(2) for spatially periodic patterns of  $\phi_A(\mathbf{x})$  and  $\phi_B(\mathbf{x})$ , optimized with respect to symmetry and unit cell dimensions [21]. We employ the PSCF code [23] to compute end-distributions for diblock morphologies at fixed segregation strengths  $\chi N$  and chain composition  $f$ .

Orientalional order of segments in block copolymer morphologies is described by two types of order parameters, both deriving spatial derivatives of end-distributions. A *polar* order parameter  $\mathbf{p}_\alpha(\mathbf{x})$  tracks the vectorial orientation of segments [16], since  $A$  and  $B$  ends are distinguishable. Assigning  $\hat{r}_\alpha$  to the orientation of segment  $\alpha$  (directed from  $A$  to  $B$  end),

$$\mathbf{p}_\alpha(\mathbf{x}) = \left\langle \rho_0^{-1} \sum_{\nu \in \alpha} \hat{r}_\alpha \delta(\mathbf{x}_\nu - \mathbf{x}) \right\rangle = \frac{V}{N} \int_\alpha dn \mathbf{J}(\mathbf{x}, n), \quad (3)$$

where the segment flux is given by  $\mathbf{J} = a(q^+ \nabla q^- - q^- \nabla q^+)/ (6Z)$ . A *nematic* order parameter  $\mathbf{Q}^\alpha(\mathbf{x})$  – a symmetric, traceless tensor – tracks anisotropy of segments consistent with head-tail symmetry (or  $\hat{r}^\alpha \rightarrow -\hat{r}^\alpha$ ) of alignment [24] (where  $i, j, k$  are spatial indices),

$$\begin{aligned} Q_{ij}^\alpha(\mathbf{x}) &= \left\langle \rho_0^{-1} \sum_{\nu \in \alpha} \left[ (\hat{r}^\alpha)_i (\hat{r}^\alpha)_j - \frac{\delta_{ij}}{3} \right] \delta(\mathbf{x}^\alpha - \mathbf{x}) \right\rangle \\ &= \frac{V}{N} \int_\alpha dn \left[ \mathcal{J}_{ij}(\mathbf{x}, n) - \frac{\delta_{ij}}{3} \mathcal{J}_{kk}(\mathbf{x}, n) \right], \end{aligned} \quad (4)$$

where  $\mathcal{J}_{ij} = a^2(q^+ \partial_i \partial_j q^- + q^- \partial_i \partial_j q^+ - \partial_i q^+ \partial_j q^- - \partial_i q^- \partial_j q^+)/ (60Z)$  (analogous expressions are derived in the SI for the Gaussian chain model). To test SCF predictions, we perform molecular dynamics (MD) simulations of analogous freely-jointed bead-spring chains, specifically using finitely extensible nonlinear elastic (FENE)

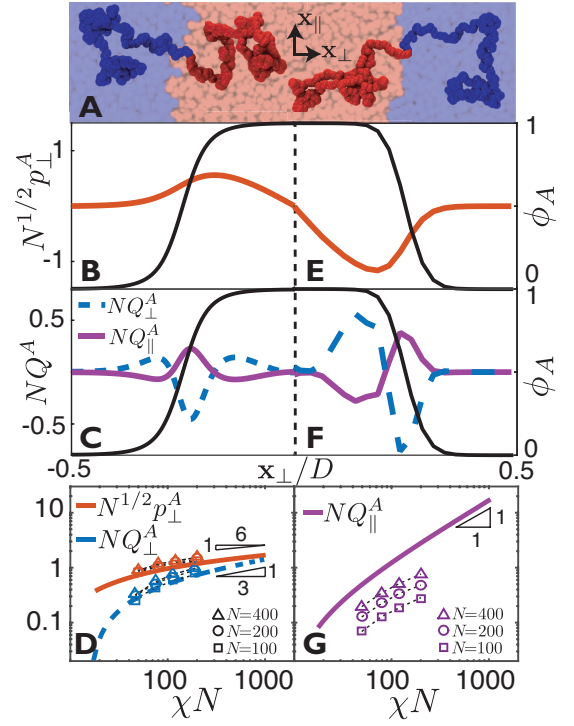


Figure 1. (A) MD snapshot showing selected chains in lamellar domains. Order parameter (left y-axis) and volume fraction (black curve, right y-axis) profiles for A-block segments in  $f = 0.5$  lamella, with (B,C) showing SCF results ( $\chi N = 30$ ) and (E,F) showing MD results ( $\chi N = 80$ ); (B,E) show the normal component of  $\mathbf{p}_A$  (parallel component is 0), and (C,F) show normal and parallel components of  $\mathbf{Q}_{ij}^A$ . Peak values of normal (D) and parallel (G) components of polar and nematic order in  $f = 0.5$  lamella are plotted vs.  $\chi N$ , with SCF results shown as curves and MD results as open symbols.

bonds and the repulsive part of the Lennard-Jones (LJ) potential for all pairwise interactions [25]. Simulations do not rely on the mean-field approximation and capture inter-segment correlation effects absent in the SCF model. Phase separation is driven by increased A-B repulsion strength  $\epsilon_{AB}$ , mapped to  $\chi_{AB}$  as in Ref [25] (see SI for details). We use a Langevin thermostat and Nosé-Hoover barostat with pressure  $5\epsilon\sigma^{-3}$ , initialize in an already microphase-separated structure and allow the box dimensions to vary to equilibrate domain spacing [26]. Vector and tensor order parameters are computed from bond-vector,  $\hat{r}_\alpha$ , distributions extracted from equilibrated configurations. Data is binned by the distance from the center of mass of lamellar or cylindrical domains (see SI for details.)

We first illustrate the basic features of “multizone” textures in lamellar morphologies. Fig. 1B,C shows SCF profiles of polar and nematic order for A-segments in well-segregated lamella at  $f = 0.5$  and  $\chi N = 30$ . Turning first to the “brush” zone deep in the A-rich domain (i.e. where  $\phi_A \approx 1$ ), we find the intuitive result of *normal* segment orientation (i.e. SmA-like). Defining  $\parallel$  and

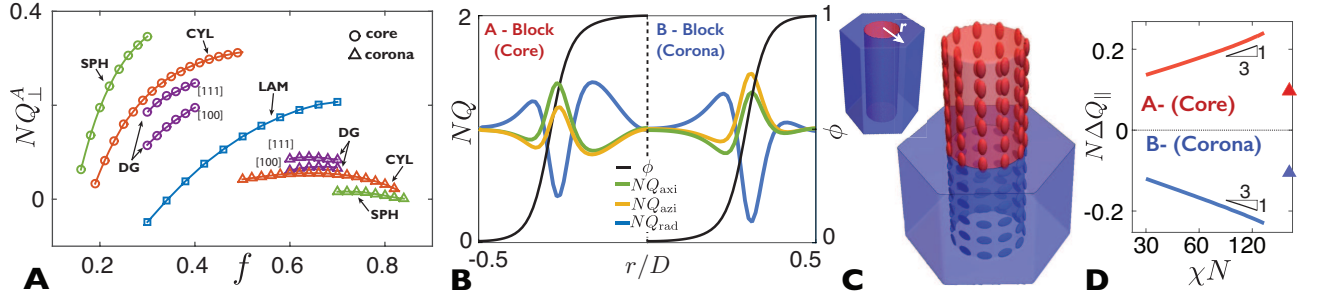


Figure 2. (A) Peak values of normal component of nematic OP for A segments,  $NQ_{\perp}^A$  in BCC spheres (SPH), hexagonal cylinders (CYL), double-gyroid (DG), and lamellar (LAM) phases. Core (corona) reflects location of A block on inner (outer) side of the AB interface. Max./min. values along both [111] and [100] axes are shown for DG (see SI.); (B) shows nematic profiles for A-(core) and B-(coronal) segments, left and right panels respectively, in the CYL phase at  $\chi N = 30$  and  $f = 0.3$ .  $Q_{axi}$ ,  $Q_{azi}$  and  $Q_{rad}$ , label the respective axial, azimuthal and radial components, defined with respect to the center axis of the cylinder with radial distance  $r$  shown in (C) inset. In (C), red and blue ellipsoids illustrate the biaxial interfacial order for core (A-block) and coronal (B-block) segments, respectively, where axes dimension reflect magnitude of  $Q_{ij}^{\alpha}$ . In (D), peak values of  $\Delta Q_{\parallel} \equiv Q_{axi} - Q_{azi}$  are plotted for SCF results (solid lines) and MD simulations (triangles) at  $f = 0.25$  for  $N = 100$ .

$\perp$  directions relative to  $AB$  interface, symmetry along the layer guarantees  $p_{\parallel}^A = 0$ , while the profile of  $p_{\perp}^A$  is odd with respect to the A-domain center, highlighting outward splay of chains away from the bilayer interfaces. In this region, the nematic order shows similar uniaxial normal alignment with  $Q_{\perp}^A > 0$  consistent with brush extension away from the  $AB$  interface. The degree of alignment can be estimated by a simple Langevin model of chains subject to a tension,  $\approx k_B T D / N a^2$ , which represents the mean-field effect of inter-segment pressure holding free ends a distance proportional to the domain width  $D$  from the interface:  $p_{\parallel}^{\alpha} \approx D_{\alpha} / (N_{\alpha} a) \sim N^{-1/2} (\chi N)^{1/6}$  and  $Q_{\perp}^{\alpha} \approx (D_{\alpha})^2 / (N_{\alpha} a)^2 \sim N^{-1} (\chi N)^{1/3}$ . Here, strong-segregation theory gives  $D_{\alpha} \sim D \approx (\chi N)^{1/6} N^{1/2} a$  [27] leading to the asymptotic  $\chi N \gg 1$  power laws observed for peak order parameters in Fig. 1D

Turning now to the interfacial zone ( $\phi_A \approx \phi_B = 1/2$ ), the nematic order parameter in Fig. 1C,F reveals that segment alignment becomes *tangential* (i.e.  $Q_{\parallel}^{\alpha} > 0$  and  $Q_{\perp}^{\alpha} < 0$ ) near the inter-domain boundary, implying that both *normal* and *tangential* segment alignment coexist within block copolymer domains, albeit at different spatial regions. The tangential alignment at the interface, though arguably less intuitive than normal ordering in the brush, is nonetheless a generic feature of the statistics of random-walks at a composition boundary, even in the absence of physical interactions that promote (inter-/intra-chain) segment alignment. This follows from the fact that segment configurations spanning from the “rich” to “poor” side of an interface are depleted relative those extending along the boundary, leading to a net bias of tangential orientations analogous to the effect of “hard wall” [28]. The degree of orientational order is directly related to the interfacial structure. End-distribution functions become independent of  $n$  near a well-segregated interface as ends and junction points are

rare. According to eq.(1) the segment distributions  $q^+$  and  $q^-$  become approximately  $\propto \sqrt{\phi_{\alpha}(\mathbf{x})}$  [29, 30]. Inserting this assumption into eq.(4) leads directly to the general form of the nematic order parameter near a sharp interface,

$$Q_{ij}^{\alpha}(\text{inter.}) = \frac{a^2}{60} \phi_{\alpha} \left[ \partial_i \partial_j \ln \phi_{\alpha} - \frac{\delta_{ij}}{3} \nabla^2 \ln \phi_{\alpha} \right], \quad (5)$$

For lamella where  $\partial_{\parallel} \phi_{\alpha} = 0$ , in the strong-segregation limit  $\partial_{\perp}^2 \ln \phi_{\alpha} \sim -\Delta^{-2}$ , where  $\Delta = a(2/3\chi)^{1/2}$  is interfacial width [27]. Hence, the strength of tangential interfacial alignment is *independent of  $N$* , scaling as  $Q_{\parallel}^{\alpha} = -Q_{\perp}^{\alpha}/2 \sim \chi$ , confirmed for peak interfacial order in lamella in Fig. 1G.

Profiles of polar and nematic order parameters from MD, in Fig. 1E,F, clearly exhibit generic features of the multizone texture predicted by SCF theory. This is despite key microscopic differences between the simulation and theory, including i) local packing constraints of finite-sized spherical monomers in the simulation absent from the SCF model, ii) non-zero compressibility of the MD model (interblock repulsion reduces interfacial density), while SCF enforces constant local density, and iii) the fact that MD simulations use relatively low  $N = 100-400$  for tractability, requiring relatively large  $\chi$  for strong segregation, while the SCF considers the limit of  $\chi \ll 1$  (or  $N \rightarrow \infty$ ). Fig. 1D,G show SCF and MD predictions are in closer agreement for normal ordering in brush than for tangential alignment at the interface, where bead-spring simulations show a weaker alignment, presumably related to the fact that  $a \gtrsim \Delta$  for sufficiently large  $\chi$ . However, we find that as  $N$  increases (at fixed  $\chi N$ ), the segment alignment in simulations tends towards SCF predictions, consistent with the approach towards  $N \rightarrow \infty$ .

Moving to curved structures, we see that interface shape has critical influence on the respective normal and

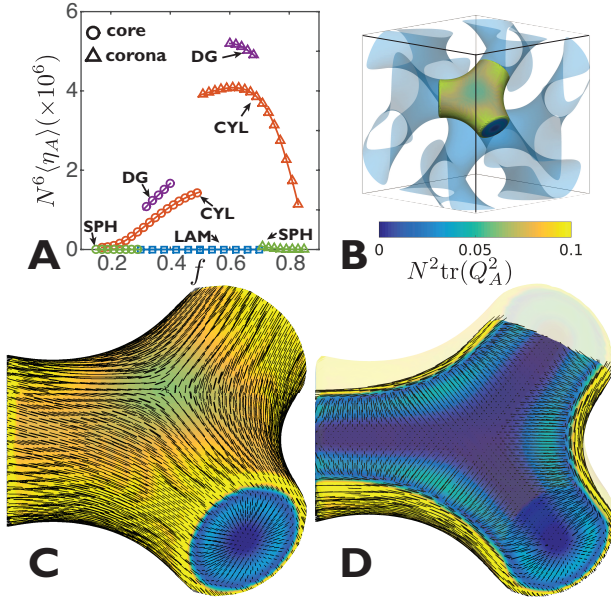


Figure 3. (A) Plot of volume-averaged biaxiality,  $\eta_A \equiv [\text{tr}(\mathbf{Q}_\alpha^2)]^2 - 54[\det(\mathbf{Q}_\alpha)]^2$ , as a function of composition  $f$  for different morphologies at  $\chi N = 30$ . (B-D) show the 3D nematic director field of the tubular minor domain of a DG network at  $f = 0.33$ , in the 3-fold region highlighted in (B). (C) shows the director profile at the interface ( $\phi = 1/2$ ), while (D) shows the profile through a core section.

tangential alignment zones. As block composition becomes increasingly asymmetric, minority block domains tend to form on the inside of the interface of increasing inward curvature [31]. By simple geometry, this leads to a tendency to *relax* the outer block length at the expense of *extending* the inner block [32]. Accordingly, normal order increases with a power of  $D_\alpha$ , such that in minority (majority) subdomains, normal alignment in brush increases (decreases) with increasing inter-domain curvature from lamella  $\rightarrow$  double-gyroid  $\rightarrow$  cylinders  $\rightarrow$  spheres, consistent with the variation of peak  $Q_\perp^A$  in Fig. 2A.

Considering alignment in the interfacial zone for morphologies with anisotropically-curved interfaces (i.e. cylinders and tubular networks), in-plane alignment couples to principle curvature axes as illustrated by the nematic order profile of a cylinder morphology in Fig. 2B. This coupling follows from the nematic order parameter,  $Q_{IJ}^\alpha \equiv \mathbf{e}_I \cdot \mathbf{Q}^\alpha \cdot \mathbf{e}_J$ , projected onto an orthonormal basis aligned to the tangent plane (spanned by  $\mathbf{e}_1$  and  $\mathbf{e}_2$ ) and the interface normal ( $\mathbf{N} = \mathbf{e}_1 \times \mathbf{e}_2$ ). Using eq.(5) and the fact that domain interfaces are isolevels of volume fraction with  $\nabla\phi_\alpha = (\partial_N\phi_\alpha)\mathbf{N}$ , the in-plane nematic order in the interfacial zone is (see SI for details)

$$Q_{IJ}^\alpha(\text{inter.}) \simeq \frac{a^2}{60} \left[ -\partial_N\phi_\alpha C_{IJ} - \frac{\delta_{IJ}}{3} (\partial_N^2\phi_\alpha - |\partial_N\phi_\alpha|^2/\phi_\alpha - 2H\partial_N\phi_\alpha) \right] \quad \text{for } I, J = 1, 2, \quad (6)$$

where  $C_{IJ} = \mathbf{N} \cdot [(\mathbf{e}_I \cdot \nabla)\mathbf{e}_J]$  is the curvature tensor [33] of the interface and  $H = (C_{11} + C_{22})/2$  is the mean curvature. For anisotropic-curved interfaces, the in-plane segment order parameter is also anisotropic, with maximal alignment along either the direction of maximal or minimal curvature. Taking  $\mathbf{e}_1$  and  $\mathbf{e}_2$  to be principal curvature directions, we measure in-plane alignment anisotropy  $\Delta Q_\parallel \equiv Q_{11} - Q_{22}$ , and find  $\Delta Q_\parallel \simeq -\frac{a^2}{60}(\kappa_1 - \kappa_2)\partial_N\phi_\alpha$ , where  $\kappa_1$  and  $\kappa_2$  are principal curvatures. Surface curvature falls with domain size as  $\kappa \propto D^{-1}$ , while  $|\partial_N\phi_\alpha| \sim D^{-1}$ , and interfacial anisotropy grows with  $N\Delta Q_\parallel \sim (\chi N)^{1/3}$  in the strong-segregation limit (shown in Fig. 2D). For cylindrical domains of core radius  $R_c$ , where  $\kappa_1 = 0$  and  $\kappa_2 = -1/R_c$  (taking  $\mathbf{N}$  to be outward),  $\partial_N\phi_\alpha$  switches sign from negative when  $\alpha$  is the inner domain to positive when it is the outer domain. Hence, not only are interfacial segments aligned to the local curvature axes, but this alignment along principal directions of  $\mathbf{Q}$  is distinct for core- vs. coronal-block segments at that interface. Peak interfacial ( $\phi \approx 1/2$ ) values of  $\mathbf{Q}$  in cylinder phases show that core-block segments align most strongly with the *axial* direction, while coronal-block segments (at that interface) align most strongly to the *coaxial* direction (shown schematically in Fig. 2C).

We note further that according to eq.(6), tangential ordering at an anisotropic interface is marked by *biaxial segment order*, with three unequal eigenvalues of  $\mathbf{Q}^\alpha$  (one negative and two unequal positive values roughly aligned to the normal and principal curvature directions of the interface, respectively). Adopting methods developed to describe biaxial phases of liquid crystals, we quantify the degree of biaxiality [34, 35] from the rotational invariant,  $\eta_\alpha \equiv [\text{tr}(\mathbf{Q}_\alpha^2)]^2 - 54[\det(\mathbf{Q}_\alpha)]^2$ , that increases from zero as eigenvalues of  $\mathbf{Q}$  become unequal. In Fig. 3A, we show biaxiality (volume averaged) of A segments,  $\langle \eta_A \rangle$ , in competing diblock phases (at  $\chi N = 30$ ), indicating that biaxial order is absent (present) for phases with isotropic (anisotropic) in-plane curvature. The negative Gaussian curvature of network interfaces [32] implies larger curvature anisotropy ( $\kappa_1 - \kappa_2$ ), and hence, the largest segment biaxiality. Fig. 3B-D, shows the complex pattern of nematic order (as illustrated by the director field) in minor, tubular domains of the double-gyroid. Notably, alignment in core brush and interfacial zone implies the formation of a point (hedgehog) and meeting at the 3-fold junction of three  $+1$  disclination-like lines that thread along the center of the tubular domains [36]. At the interface, locking of the director to the curvature axes leads to the formation of two  $-1/2$  disclinations on antipodal points of the three-fold junction that localize the conflict with in-plane order and Gaussian curvature of the interface.

To conclude, while the degree of normal alignment of brush segments increases inversely with chain length



( $\sim N^{-1/3}$  and  $\sim N^{-2/3}$  for polar and nematic order, respectively), we find that tangential alignment at the interface is independent of chain length and grows in proportion to  $\chi$ . This suggests that even in flexible diblocks, tangential alignment approaches significant levels ( $Q_{ij} \sim 1$ ) in high- $\chi$  systems [37, 38]. Notably, the flexible chain model here includes no orientational interactions between segments, and hence, the induced ordering within microdomains falls outside of Onsager description of lyotropic chain alignment [39]. The texture exhibited by flexible diblocks is a necessary reference point for studying orientational order in systems with additional tendencies promoting intra-chain (i.e. persistence) and inter-chain segmental alignment [16, 17, 40–42]. For example, recent studies of BCPs with chiral polymer blocks [43] suggest these systems may be described by an additional preference of twisted (e.g. cholesteric) packing in the chiral micro domains [44–46], a pattern of gradient orientation that competes with the entropically favorable multi-zone alignment described here. Finally, we note that segment alignment at anisotropic inter-domain surfaces may have key, yet unexplored consequences for behavior of functional BCPs; e.g. materials where functionality emerges from the interface and relies on directional processes (e.g. optical response, charge transport) will exhibit a strong dependence on core vs. coronal placement of functional blocks.

We are indebted to A. Arora for key input regarding the implementation of PSCF, and to E. Thomas and R. Kamien for valuable discussions. This work was supported by U.S. Department of Energy, Office of Science, Office of Basic Energy Sciences, under Award Number DE-SC0014549 (SCF theory, IP and GG) and National Science Foundation under Grant No. 1454343 (MD simulations, YS and LMH), using computational facilities at the Massachusetts Green High Performance Computing Center and the Ohio Supercomputer Center.

---

[1] F. S. Bates and G. H. Fredrickson, *Annu. Rev. Phys. Chem.* **41**, 525 (1990).  
[2] G. M. Grason, *Physics Reports* **433**, 1 (2006).  
[3] V. Abetz and P. F. W. Simon, *Adv. Polym. Sci.* **189**, 125 (2005).  
[4] M. W. Matsen, *Macromolecules* **189**, 2161 (2012).  
[5] M. W. Matsen, *Journal of Physics: Condensed Matter* **14**, R21 (2002).  
[6] I. W. Hamley, *Nanotechnology* **45**, R39 (2003).  
[7] O. D. Lavrentovich and E. M. Terentjev, *Sov. Phys. JETP* **64**, 1237 (1986).  
[8] A. Fernandez-Nieves, V. Vitelli, A. S. Utada, D. R. Link, M. Marquez, D. R. Nelson, and D. A. Weitz, *Phys. Rev. Lett.* **99**, 157801 (2007).  
[9] F. Serra, K. C. Vishnubhatla, M. Buscaglia, R. Cerbino, R. Osellame, G. Cerullo, and T. Bellini, *Soft Matter* **7**, 10945 (2011).

[10] D. Sec, Porenta, Ravnik, and S. Zumer, *Soft Matter* **8**, 11982 (2012).  
[11] J. A. Martinez-Gonzalez, T. Zhou, M. Rahimi, Bukusoglu, N. L. Abbott, and J. J. de Pablo, *Proc. Nat. Acad. Sci. USA* **112**, 13195 (2015).  
[12] M. Kléman and O. D. Lavrentovich, *Soft Matter Physics, An Introduction* (Springer, 2003).  
[13] I. Szleifer and B. Widom, *J. Chem. Phys.* **90**, 7524 (1989).  
[14] J.-P. Carton and L. Leibler, *Journal de Physique* **51**, 1683 (1990).  
[15] D. C. Morse and G. H. Fredrickson, *Phys. Rev. Lett.* **73** (1994).  
[16] W. Zhao, T. P. Russell, and G. M. Grason, *J. Chem. Phys.* **137**, 104911 (2012).  
[17] Y. Jiang and J. Z. Y. Chen, *Phys. Rev. Lett.* **110**, 138305 (2013).  
[18] M. Doi and S. F. Edwards, *The Theory of Polymer Dynamics* (Oxford, 1986).  
[19] Here, we take the limit  $N \rightarrow \infty$  and  $a \rightarrow 0$  with  $N^{1/2}a$ , such that large-scale structure is described by Gaussian walk statistics.  
[20] E. Helfand, *J. Chem. Phys.* **62**, 999 (1975).  
[21] G. Fredrickson, *The Equilibrium Theory of Inhomogeneous Polymers*, 134 (Oxford University Press, 2006).  
[22] End-distributions satisfy spatially uniform initial conditions,  $q^+(n=0) = q^-(n=N) = 1$ .  
[23] A. Arora, J. Qin, D. C. Morse, K. T. Delaney, G. H. Fredrickson, F. S. Bates, and K. D. Dorfman, *Macromolecules* **49**, 4675 (2016).  
[24] P.-G. de Gennes and J. Prost, *The Physics of Liquid Crystals*, 2nd ed. (Oxford, 1993).  
[25] G. S. Grest, M.-D. Lacasse, K. Kremer, and A. M. Gupta, *J. Chem. Phys.* **105**, 10583 (1996).  
[26] Y. Seo, J. R. Brown, and L. M. Hall, *Macromolecules* **48**, 4974 (2015).  
[27] A. N. Semenov, *Sov. Phys. JETP* **61**, 733 (1985).  
[28] The distribution of interfacial orientation follows directly as the probability  $\rho(\mathbf{x}, \hat{r})$  of segment orientation  $\hat{r}$  at  $\mathbf{x}$  that *any two* (like) chain sections span from  $\mathbf{x} - a\hat{r}/2$  to  $\mathbf{x} + a\hat{r}/2$ . In other words, the probability  $\rho(\mathbf{x}, \hat{r})$  is the *geometric mean* of segment density at nearby points,  $\rho(\mathbf{x}, \hat{r}) \simeq \sqrt{\phi(\mathbf{x} - a\hat{r}/2)} \times \sqrt{\phi(\mathbf{x} + a\hat{r}/2)}$ . Because  $\ln \phi(\mathbf{x})$  necessarily becomes non-convex at the interface (along the normal direction,  $\mathbf{N}$ ), fewer orientations span perpendicular ( $\perp$ ) than parallel ( $\parallel$ ) to the AB interface,  $\rho_{\perp}(\mathbf{x}) - \rho_{\parallel}(\mathbf{x}) \simeq (a^2/8)\phi \partial_{\mathbf{N}}^2 \ln \phi < 0$ .  
[29] E. Helfand and Z. R. Wasserman, *Macromolecules* **9**, 879 (1976).  
[30] J. L. Goveas, S. T. Milner, and W. B. Russel, *Macromolecules* **30**, 5541 (1997).  
[31] M. W. Matsen and F. S. Bates, *Macromolecules* **29**, 7641 (1996).  
[32] P. D. Olmsted and S. T. Milner, *Phys. Rev. Lett.* **72**, 936 (1994).  
[33] R. D. Kamien, *Rev. Mod. Phys.* **74**, 953 (2002).  
[34] M. J. Freiser, *Physical Review Letters* **24**, 1041 (1970).  
[35] R. Alben, *Phys. Rev. Lett.* **30**, 778 (1973).  
[36] G. P. Alexander, B. G. G. Chen, E. A. Matsumoto, and R. D. Kamien, *Reviews of Modern Physics* **84**, 497 (2012), arXiv:1107.1169.  
[37] D. P. Sweat, M. Kim, S. R. Larson, J. W. Choi, C. O. Osuji, and P. Gopalan, *Macromolecules* **47**, 6687 (2014).  
[38] W. J. Durand, G. Blackout, M. J. Maher, S. Sirard,

- S. Tein, M. C. Carlson, Y. Asano, S. X. Zhou, A. P. Lane, C. M. Bates, C. J. Ellison, and C. G. Willson, *J. Polym. Sci. Part A: Polym. Chem.* **15**, 344 (2015).
- [39] A. R. Khokhlov and A. N. Semenov, *J. Stat. Phys.* **38**, 161 (1985).
- [40] M. W. Matsen, *J. Chem. Phys.* **104**, 7758 (1996).
- [41] D. Duchs and S. D. E., *J. Phys.: Condens. Matter.* **14**, 12189 (2002).
- [42] L. Shibin, Y. Jiang, and J. Z. Y. Chen, *J. Chem. Phys.* **145**, 184902 (2016).
- [43] R.-M. Ho, Y. W. Chiang, C. K. Chen, H. W. Wang, H. Hasegawa, S. Akasaka, E. L. Thomas, C. Burger, and B. S. Hsiao, *J. Am. Chem. Soc.* **30**, 1439 (2009).
- [44] W. Zhao, T. P. Russell, and G. M. Grason, *Phys. Rev. Lett.* **110**, 058301 (2013).
- [45] S. Wang, T. Kawakatsu, P. Chen, and C. D. Lu, *J. Chem. Phys.* **138**, 194901 (2013).
- [46] G. M. Grason, *ACS MacroLett.* **4**, 526 (2015).